

Chapter 5

Pulsar-Gated Radio Imaging of Young PM Survey Pulsars

5.1 Introduction

We have observed fields containing seven young pulsars which have been discovered in the Parkes Multibeam Pulsar Survey (PM Survey) (described in Chapter 2). All of these pulsars have southern declinations ($-64^\circ < \delta < -54^\circ$) and were observed with the Australia Telescope Compact Array (ATCA).

5.1.1 Motivation for Pulsar-Gated Imaging

Pulsar-gated radio imaging of young pulsars is important for several reasons. The primary motivation for using this technique is to establish with certainty the positions of pulsars. The purpose of this is two-fold. First, accurate positions are sometimes necessary for obtaining timing solutions, particularly for young pulsars which can exhibit timing noise. Timing noise, explained in Chapters 1 and 4, can prevent a timing solution from being obtained since it introduces deviations in the spin-down behavior which cannot be modeled and accounted for. With accurate positions, the timing solution has fewer free parameters and can more easily be constrained.

The second reason for obtaining accurate positions with gating is to establish as-

sociations with extended radio objects. This is also particularly relevant for young pulsars, which can be associated with supernova remnants (SNRs) or pulsar wind nebulae (PWNe). The motivation for finding and studying such associations is presented in Chapter 1. Sensitivity to PWNe can also be enhanced with pulsar gating by allowing the pulsed flux to be subtracted from the image, thereby increasing sensitivity to faint underlying emission. Spectral index information can also be obtained from imaging to help identify objects as sources with a non-thermal emission mechanism. Chapter 6 discusses this in further detail.

5.1.2 Radio Interferometry

The following description follows the one presented in the ATCA User’s Guide.¹

For the radio imaging work on the pulsars in this chapter, we have used the ATCA, an earth-rotation aperture synthesis radio interferometer. Earth-rotation aperture synthesis is explained in detail elsewhere (Clark 1989; Thompson, Moran, & Swenson 1986). In radio synthesis observations, the antennas of the array are used in pairs to form interferometers. By correlating the signals from each antenna pair, called a baseline, one measures the fraction of the signal which is common to both antennas in the pair.

Combining these correlated signals obtained over a long period of time and using a large range of antenna spacings yields a measurement of the spatial coherence function throughout a range of values in the u - v plane, which is the Fourier plane to the sky image plane. The spatial coherence function V is the Fourier transform of the sky intensity distribution:

$$V(u, v) = \int I(\hat{s}) e^{(2\pi i \hat{s} \cdot (\vec{r}_i - \vec{r}_j) / \lambda)} d\Omega. \quad (5.1)$$

Here $I(\hat{s})$ is the two dimensional intensity distribution on the sky, \hat{s} is the unit vector in the direction of the pointing center toward the celestial source, $(\vec{r}_i - \vec{r}_j)$ is the separation vector between antenna pair ij , and $d\Omega$ indicates integration over the

¹<http://www.narrabri.atnf.csiro.au>.

celestial sphere. This expression assumes that the radiation is monochromatic with wavelength λ .

By Fourier transformation of the spatial coherence function, an image of a radio source is produced. This image is convolved with the sampling function determined by the aperture coverage in the u - v plane, and the image must be deconvolved from this sampling function to recover the true intensity distribution. The image formed has the same angular resolution as would be obtained for an image with a single antenna with a diameter equal to the largest baseline separation.

5.1.3 The Australia Telescope Compact Array

The ATCA consists of six 22-m radio antennas located near Narrabri, NSW, Australia (Frater, Brooks, & Whiteoak 1992). Five of the six antennas lie along a three-kilometer railway track, which is oriented east-west. The sixth antenna lies on a 75-m rail-track three kilometers further west, thus allowing a maximum baseline of 6 km. These antennas can be moved along the railway tracks and positioned at any of 37 fixed stations, each of which contains a port that allows the data from the antenna to be transferred to the control building. Due to the location of the stations and other physical constraints, the shortest baseline possible is ~ 30 m.

The antennas are regularly moved to different stations, corresponding to different array configurations used for observing. An observation length of 12 h fully covers the possible spacings in the u - v plane for a given configuration. By observing a given source using multiple configurations and combining the separate u - v data sets, one can get more complete u - v coverage for the sampling function and generally make better images.

Each of the six antennas has an altitude-azimuth mount and a Cassegrain design, with receivers located at the main reflector surface. The feeds are mounted along the main optic axis, allowing observations to be made in two simultaneous orthogonal linear polarizations with low ($\sim 1\%$) instrumental polarization. Each antenna has receivers which are sensitive to four radio frequencies centered at roughly 1.5, 2.4, 5.3, and 8.5 GHz. There are two feeds mounted on each antenna, one of which is

sensitive to radiation at both 1.5 GHz and 2.4 GHz and one at both 5.3 GHz and 8.5 GHz. Each feed has a separate receiver for each of the two frequencies. All receivers run continuously and use cooled FET and HEMT amplifiers that provide wide bandwidths and total system temperatures between 30 K to 65 K, depending on the frequency.

The received signals are amplified and downconverted by mixing with a signal from a local oscillator. The ATCA allows simultaneous observations of both polarizations at the two available frequencies in either dual-receiver system. The center frequencies can be anywhere in the range covered by the selected feed. After downconversion, the signals from each antenna are digitized using two-bit sampling and sent to a correlator. A synchronizing code is added to the data stream from each antenna at the start of each integration cycle to allow each bit in the signal stream to be correctly identified at the correlator.

The correlator compares simultaneous signals from the two data streams from each antenna pair: if the signal from both antennas is in the same state, then the signals are correlated. A plane wavefront approaching the array will, in general, arrive at different antennas at different times due to a geometric delay between the antennas. The signals from the antennas therefore need to be delayed before being presented to the correlator to account for this delay and to account for additional delays from path length differences and instrumental variations.

The output from the correlator for each antenna pair (baseline) is the cross-correlation (lag) function of the signals from the two antennas, which is the Fourier transform of the cross-power spectrum of the two signal streams. This correlator output is then sent to a computer which Fourier transforms the cross-correlation function to recover the (complex) cross-power spectrum for each baseline. Data are averaged for the integration cycle and then written to disk. For our observations, we used an integration cycle time of 40 s. These complex values are the visibilities in the u - v plane which sample the spatial coherence function. A radio image can then be constructed from the measured spatial coherence function by taking the Fourier transform of the function and deconvolving the resulting image. This step is neces-

sary since the spatial coherence function cannot be perfectly sampled by the baseline tracks in the u - v plane.

5.1.4 Pulsar Gating

In normal interferometric radio observations described above, each baseline is integrated for the cycle (in our case 40 s) and a single complex correlation value is obtained for each baseline, representing a single point in the u - v plane. The pulsar gating feature of the ATCA can be used to separately record data for each phase bin of the pulsar's profile. Using an ephemeris for the pulsar, a topocentric pulsar period is determined over the course of the observation. This period will vary slightly over the course of the observation but is constant for each integration cycle. During observing, each integration cycle is split into an integral number of pulse periods, each of which in turn is split into (typically) 32 bins. Each bin is integrated separately, and at the end of the integration cycle, a complex correlation value is output for each phase bin of the profile. Using this technique, the separately recorded binned data can then be grouped into on and off-pulse data, thereby allowing two maps to be made from the two data sets, with the difference that the pulsed emission appears at the pulsar's location in only one of the maps. A comparison of the maps reveals the pulsar's position, and a map made from the off-pulse data set provides an increased sensitivity to faint underlying emission at the pulsar's location. Figure 5-1 shows on and off-pulse maps for PSR J1119–6127, using data from only the 6D array configuration. The pulsar is clearly seen as a point source in the on-pulse image and does not appear in the off-pulse image.

5.2 Observations and Data Reduction

Each of the seven pulsar fields we have observed had a southern declination ($\delta < -50^\circ$). We therefore used the ATCA in several configurations for these observations. Typical integrations were about 12 h in each configuration. Two 128-MHz bandwidths (split into 32×4 -MHz frequency channels) were simultaneously observed, centered

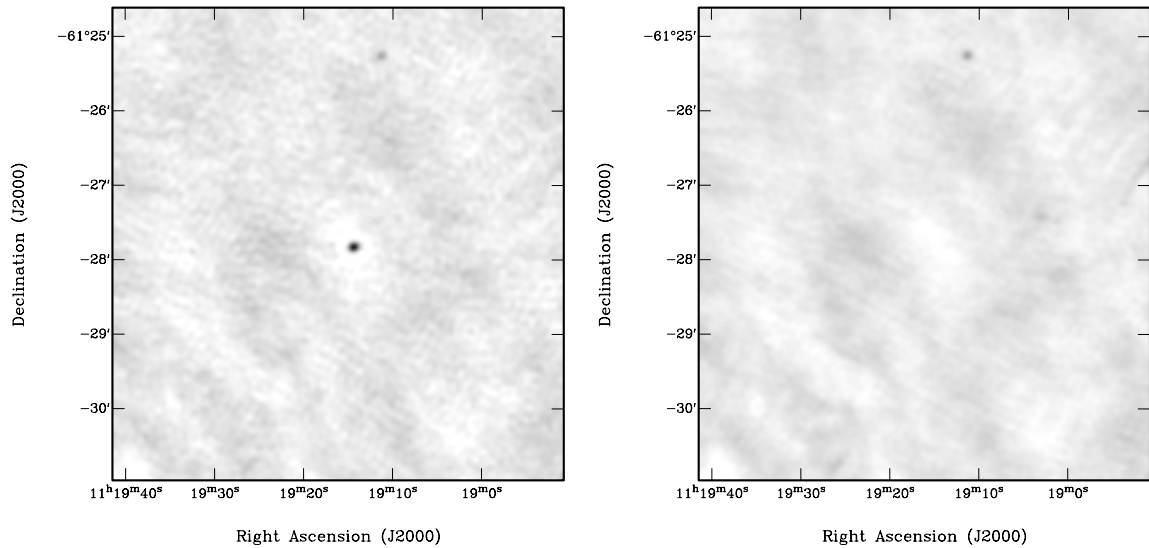


Figure 5-1 1.4-GHz maps of the region containing PSR J1119–6127 made with on-pulse (left) and off-pulse (right) data from gating. The only feature (aside from noise) which is different in the two maps is the pulsar, which appears as a point source.

on radio frequencies of 1.4 GHz and 2.5 GHz. Each of the 32 frequency channels was sensitive to full Stokes parameters for each baseline. Table 5-1 lists the observing parameters for each of the observations.

Using the MIRIAD² data reduction package (Sault & Killeen 1998), the data were first edited for radio frequency interference (RFI). The amplitudes of every point in the u - v plane are checked for excessively large values, which would clearly indicate the presence of RFI. These data were removed (flagged). The remaining data were then phase calibrated and flux calibrated using the sources listed in Table 5-1. Phase calibration determines a time-dependent gain function for each antenna in the array. Both phase and amplitude corrections based on these gain functions are then applied to the recorded u - v data. Phase calibration also determines the instrumental polarization as a function of time and corrects for this. In flux calibration, an overall scale factor (which is tied to the flux density of a well-known source) is applied to the u - v data.

In the observations with the highest spatial resolutions, we used pulsar gating

²<http://www.atnf.csiro.au/computing/software/miriad>.

Table 5-1. ATCA Observing Parameters for Seven Pulsars

PSR	Observing Dates	Array Config	PKS Phase Calibrator	PKS Flux Calibrator	Integration Time (h)
J0940–5428	1999 Aug 18-19	6D ^a	0823–500	1934–638	6.8
J1112–6301 ^b	1999 Nov 28-29	0.375	1036–697	1934–638	12.9
	1999 Dec 16	1.5A ^a	1036–697	1934–638	12.4
J1119–6127	1998 Oct 30-31	6D ^a	1036–697	1934–638	12.8
	1998 Nov 1 ^c	6D	1036–697	1934–638	7.6
	1999 Nov 25-26	0.375	1036–697	1934–638	12.8
	1999 Dec 14	1.5A	1036–697	1934–638	13.0
J1301–6305	1999 Aug 22-23	6D ^a	1329–665	1934–638	10.6
	1999 Dec 15-16	1.5A	1329–665	1934–638	12.4
J1413–6141 ^d	1998 Nov 1	6D ^e	1329–665	1934–638	8.8
	1998 Nov 1-2	6D ^e	1329–665	0823–500	4.6
	1999 Nov 27-28	0.375	1329–665	1934–638	13.1
	1999 Dec 17-18	1.5A	1329–665	1934–638	12.6
J1420–6048	1999 Aug 20-21	6D ^a	1329–665	1934–638	11.5

Unless otherwise specified, data were taken at center frequencies of 1384 MHz and 2496 MHz with 32 phase bins used in the gating. 128-MHz bandwidths were used for each frequency in each observation.

^aGating results used to estimate a position and flux density.

^b16 phase bins used in gating.

^cCenter frequencies of 1344 MHz and 2240 MHz used.

^dPSR J1412–6145 also included in these observation fields.

^eGlitch activity prevented successful gating.

to separately record data for each of 32 phase bins of the pulsar’s profile. In the case of PSR J1112–6301, the gating hardware could only accommodate 16 bins due to the fast period of the pulsar. The bins for each frequency channel were phase adjusted to account for the effect of dispersion using the MIRIAD task PSRFIX. Since the dispersion measure (DM) for each pulsar is known prior to observation, the dispersive time delay of the pulse in each of the frequency channels is known. This can be converted into a pulse phase delay by dividing the time delay by the pulsar period P , which is also known. The adjusted phase bins were grouped into on and off-pulse data. In two cases pulsar gating was not used. PSRs J1412–6145 and J1413–6141 were in the same field, and gating on PSR J1413–6141 was attempted. However, since this pulsar had glitched, an accurate topocentric pulse period was not obtained.

5.3 Position and Flux Density Results

From the gated data we made on and off-pulse u - v data sets. The off-pulse u - v data set was subtracted from the on-pulse data set, leaving only the pulsar’s pulsed signal in the presence of noise. We then used the UVFIT procedure in MIRIAD to find a best-fit point source position and flux density in the u - v data set with uncertainties in this fit. The fitted positions had an additional uncertainty from the position uncertainty of the phase calibrators. The calibrator with the most poorly determined position, PKS 1036–697, had an uncertainty less than $0.1''$ (N. Tasker, unpublished work). Adding in quadrature the positional uncertainty from the fit with that of the phase calibrator yielded a best-fit gated position for each pulsar. This position was checked for consistency against the position of the pulsar roughly determined from a comparison of maps made with the on and off-pulse data (Figure 5-1).

These interferometric positions were then used for the pulsar positions in the timing solution. Once sufficiently accurate model parameters were obtained in each timing solution, the position was allowed to vary in the fit to fully minimize the residuals. In several cases a second frequency derivative was introduced in the timing

solution to maintain consistency between the timing model position and the position from gating. Table 5-2 lists the best-fit positions from the pulsar gating and from the final timing solutions for comparison. In the case of PSRs J1412–6145 and J1413–6141, positions were estimated from point-source positions in the maps. In two cases (PSRs J0940–5428 and J1420–6048) there are minor discrepancies in the declination values estimated from the two methods. This can be attributed to timing noise, which is prevalent among young pulsars.

Due to timing noise and a degeneracy between the astrometric and spin parameters, a timing solution was obtained for PSR J1119–6127 which was incorrect. ATCA gated observations of this pulsar were used to break this degeneracy by establishing the position with certainty. Once the position was established, a correct timing solution was determined which included a braking index. The timing results for PSR J1119–6127 are presented along with a full discussion of the procedure elsewhere (Camilo et al. 2000).

The best-fit flux density from UVFIT was also recorded. An additional 5% uncertainty in the flux density was added in quadrature to the UVFIT flux density uncertainty. This conservatively accounts for the uncertainty in the flux calibration. Table 5-3 lists the flux density estimates from both the 1.4-GHz and 2.5-GHz data. In most cases the spectral index α could also be estimated, though with a large uncertainty. For PSRs J1412–6145 and J1413–6141, flux densities were estimated from the flux densities of point-sources in the maps at the pulsar location.

We have used the estimated 1.4-GHz flux densities to check the PM Survey sensitivity calculation presented in Chapter 2. This check is described in Chapter 2.

Table 5-2. ATCA Position Estimates for Seven Pulsars

PSR	Freq (MHz)	Array Config	Gated Position ^a	Timing Position ^a	σ^b
J0940–5428	1384	6D	$\alpha = 09:40:58.258(15)$ $\delta = -54:28:39.78(23)$	$\alpha = 09:40:58.22(4)$ $\delta = -54:28:40.6(3)$	0.9 2.2
J1112–6103	2496	1.5A	$\alpha = 11:12:14.859(86)$ $\delta = -61:03:31.74(65)$	$\alpha = 11:12:14.81(4)$ $\delta = -61:03:31.1(6)$	0.5 0.7
J1119–6127	1384	6D	$\alpha = 11:19:14.300(21)$ $\delta = -61:27:49.48(15)$	$\alpha = 11:19:14.24(5)$ $\delta = -61:27:49.8(5)$	1.1 0.6
J1301–6305	1384	6D	$\alpha = 13:01:45.725(27)$ $\delta = -63:05:34.48(23)$	$\alpha = 13:01:45.8(1)$ $\delta = -63:05:34(1)$	0.7 0.5
J1412–6145 ^c	1384	6D	$\alpha = 14:12:08(1)$ $\delta = -61:45:29(4)$	$\alpha = 14:12:07.69(5)$ $\delta = -61:45:28.8(6)$	0.3 0.1
J1413–6141 ^c	1384	6D	$\alpha = 14:13:10(1)$ $\delta = -61:41:13(4)$	$\alpha = 14:13:09.87(9)$ $\delta = -61:41:13(1)$	0.1 0.0
J1420–6048	2496	6D	$\alpha = 14:20:08.237(16)$ $\delta = -60:48:16.43(15)$	$\alpha = 14:20:08.3(1)$ $\delta = -60:48:18.1(9)$	0.6 1.8

Figures in parentheses represent 1σ uncertainties in the least-significant digit quoted.

^aJ2000 positions in units of hours:minutes:seconds for right ascension (α) and degrees:arcminutes:arcseconds for declination (δ).

^bDiscrepancy in the values obtained from gating and timing.

^cNo pulsar gating used. Position obtained from point-source position in map.

Table 5-3. ATCA Flux Density Estimates for Seven Pulsars

PSR	Freq (MHz)	Array Config	Flux Density (mJy)	α^a
J0940–5428	1384	6D	0.66(4)	+0.7(3)
	2496		0.98(12)	
J1112–6103	1384	1.5A	0.54(13)	–1.3(8)
	2496		0.25(5)	
J1119–6127	1384	6D	1.02(7)	–1.4(3)
	2496		0.44(5)	
J1301–6305	1384	6D	0.47(9)	–0.9(6)
	2496		0.28(4)	
J1412–6145 ^b	1384	6D	0.6(3)	–
	2496		0.2(2)	
J1413–6141 ^b	1384	6D	0.8(4)	–
	2496		0.4(2)	
J1420–6048	1384	6D	1.09(8)	–1.0(7)
	2496		0.61(17)	

Figures in parentheses represent 1σ uncertainties in the least-significant digit quoted.

^aSpectral index α determined from 1.4-GHz and 2.5-GHz flux density measurements, where $S \sim \nu^\alpha$.

^bNo pulsar gating used. Flux density obtained from point-source flux density in map.

